

Fabrication and SERS Study of Single Silver Nanoparticles

Tong Xiao, Qi Ye and Li Sun*

Department of Chemistry, University of Minnesota, Minneapolis, MN

Abstract

A new method based on scanning-tunneling-microscope (STM) lithography was developed to fabricate single Ag nanoparticles on atomically flat Au(111) surfaces. The method was also used to transfer simple patterns as trench structures on Au(111) surfaces. Surface-enhanced Raman scattering (SERS) from probe molecules adsorbed on the surface of nanoparticles was quantitatively measured to reveal the relationship between the spatial distribution of particles and the enhancement of local electromagnetic (EM) field. Extra enhancement due to particle clustering was observed.

Introduction

We describe a new method for fabricating single Ag nanoparticles in a well-controlled manner. These particles are useful models for studying a variety of chemical and physical processes on the nanometer scale. For example, we have detected SERS from one single nanoparticle and gained new insight about SERS mechanism.

Nanostructured materials have attracted a great deal of interests recently¹. Their advantages over conventional materials include superior mechanical strength and ductility, flexibility and low cost in material processing, easy tailoring of optical properties, efficient molecular transport, and large surface areas for catalytic and photochemical applications. Commercialization of nanomaterials demands economic methods of production on a large scale. However, it is sometimes desirable to produce well-defined single particle models for fundamental understanding of various properties of nanoparticles. Our approach presented here will allow one to investigate systematically the effects of particle morphology (size, shape, and distribution) on particle properties. In comparison, traditional methods of characterizing an ensemble of particles only provide statistically averaged results, thus they are ineffective for evaluating the effects of particle morphology.

SERS is a good example to show that EM field enhancement is a sensitive function of surface roughness or particle morphology. Although SERS has been known for about 20 years, its mechanism is still not completely understood². EM field enhancement is believed to be the dominant mechanism; however, its quantitative evaluation is difficult because of the lack of well-defined experimental models. In addition, a short range chemical enhancement

mechanism further complicates the above task. Previous SERS studies rely on models that contain aggregates of particles. Although monodispersed particles can be obtained, significant variations still remain. In addition, the effects of particle shape and spacing cannot be quantitatively evaluated if the enhancement due to an isolated single particle is unknown. We and others have shown that single particle SERS experiments are highly informative about the enhancement mechanism^{3,4}.

Experimental Section

Water of 18.2 megohm-cm resistivity and chemicals of analytical grade or better were used in all procedures. The Raman probe, *trans*-4-mercaptomethyl stilbene (*t*-4MMS), was synthesized previously.³ The electrochemical and Raman spectroscopic measurement systems have also been described previously.³ Routine data acquisition parameters were 400 μm slit width, 2 mW laser power (647.1 nm), and 50 s integration time. Samples were mounted with their Au(111) facets perpendicular to the incident beam, and sample position relative to the focal point was controlled by a xyz translational stage equipped with manual micrometers of 0.5 μm resolution. All topographic images were obtained with a Nanoscope III scanning probe microscope vibration-isolated with the "bungee" cord design.⁵ The STM tips were mechanically cut from a 0.010"-diameter Pt/Ir (80/20 w%) wire while tips for a scanning force microscope (SFM) were pyramidal Si_3N_4 cantilevers with a spring constant of 0.58 N/m. Typical STM imaging conditions were 300 mV bias voltage, 0.11 nA constant tunneling current, and 2 Hz scan rate. Typical SFM conditions were 2-Hz scan rate and constant force mode. Au(111) surfaces were prepared and cleaned according to literature procedures.⁶

Figure 1 illustrated the method for single particle fabrication. After the last step of fabrication, Raman scattering from a single Ag particle was measured first, followed by SFM measurements of the particle topography.

Results and Discussions

STM Lithography and Single Particle Fabrication

The first step in the fabrication of single Ag particles involves pattern creation via STM lithography. The lithographic procedure was first reported by Ross *et al.* who showed that a STM tip can selectively remove chemisorbed

alkanethiol molecules, resulting in an increased electron transfer rate at the tip-etched area.⁷ To increase the electron transfer rate further, we have added an extra cyanide etching step which removes any residue alkanethiol molecules within the tip-etched area. Cyanide etching is a highly selective process: only the monolayer defects or regions not covered by alkanethiols are etched.⁸

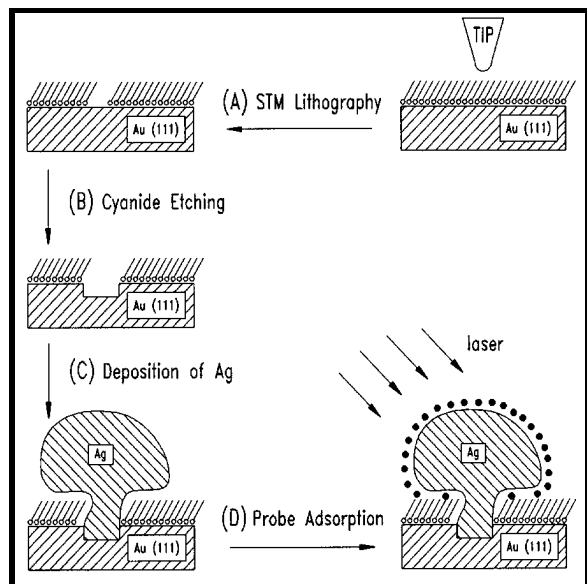


Figure 1: Fabrication of single Ag nanoparticles. An Au(111) was covered with a self-assembled monolayer (SAM) of hexadecanethiol by soaking in a 1 mM ethanolic thiol solution. (A) The SAM-covered Au(111) was etched via STM lithography in air with typical conditions of 3 to 5 V bias voltage, 0.11 nA tunneling current, 30 to 40 Hz scan rate, and 3 min etching time. (B) The sample was etched further by electrochemical anodization in a solution of 0.1 M Na_2HPO_4 and 0.1 M NaCN at 300 mV (vs. an Ag/AgCl/3M NaCl reference electrode purchased from BAS, West Lafayette, IN) for 10 s. (C) After rinse with water, the sample was transferred to another electrolyte containing 1 mM AgClO_4 and 0.1 M HClO_4 , followed by Ag deposition at a suitable potential (vs. a home-made Ag/AgCl/saturated-KCl reference electrode with a 0.1 M HClO_4 bridge). (D) Finally, the sample was rinsed with water and absolute ethanol, and soaked immediately in 1 mM ethanolic t-4MMT solution for 20 min.

Figure 2A shows a typical STM image of a SAM-covered Au(111) surface. The small pits, manifested as small dark spots in the image, have been investigated previously by several research groups.^{9,10} The most detailed study so far indicates that these pits may result from the lifting of Au(111) surface reconstruction upon thiol adsorption.¹⁰ Figure 2B illustrates the surface topography of the same area after a 50 nm \times 50 nm square crater is created via STM lithography. The depth of the crater and its uniformity are determined by many factors. For example, increasing the scan rate improves uniformity, and longer etching time results in a deeper crater. However, quantifying the above observations is difficult. In fact, sometimes we could not

even produce any crater pattern under our standard conditions. We did not understand the irreproducibility of STM lithography until we learned recently that humidity is a critical factor and that an electrochemical mechanism similar to the cathodic thiol desorption is responsible for thiol removal by the scanning STM tip.¹¹ The humidity is important because it promotes the formation of a thin-film electrolyte between the tip and the surface below it. This explanation is strongly supported by our data. Although we did not record humidity, we were able to estimate it from the hourly-humidity data obtained from a local newspaper.¹² Without exception, all of our successful lithography experiments were performed during rainy days when the outdoor humidity was above 90% and the temperature ranging from 10 C to 27 C. We expect that the indoor humidity would approximately track the outdoor humidity although the absolute value might be different because of the outdoor/indoor temperature difference and the variation in ventilation efficiency.

The main purpose of STM lithography is to spatially modulate the rate of Ag deposition. Our original plan was to use a tip-etched area as a microelectrode from which an Ag particle could grow. However, this approach was not successful because there was not enough contrast between the Ag deposition rate at the tip-etched area and the rates elsewhere. We think that the lack of contrast is due to the incomplete removal of thiols from tip-etched area, which results in a higher overpotential for initial Ag deposition. The observed threshold potential varied randomly for different samples from 0 to 400 mV, a range more negative than the theoretical threshold for bulk Ag deposition from a 1 mM Ag^+ solution—about 425 mV vs. an Ag/AgCl/KCl (sat.) reference electrode. One consequence of using a large overpotential is that Ag deposition also occurs at the adventitious defect sites within the SAM layer. Therefore, in many failed experiments, whenever we observed Ag deposition at the tip-etched area, we also observed it over unetched areas.

We have attempted to remove the residue thiols in the tip-etched area by oxidizing it at 1100 mV just before Ag deposition.¹³ However, this anodic excursion enhances Ag nucleation at the adventitious defects, resulting in a decreased contrast in Ag deposition rate. The Ag particle density is so high that it is impossible to find features due to STM lithography (Figure 3). The second strategy we have used to enhance the contrast in Ag deposition rate involves removing the residue thiols by electrochemically controlled cyanide etching. This operation also etches adventitious defects,⁸ however, the contrast in cyanide etching rate is much larger than that for Ag deposition. Figure 4 shows a STM-etched surface after cyanide etching. The etching time for the image in Figure 4 is much longer than the time needed to remove the residue thiol molecules (3 min vs. 10 s). We choose this image deliberately to show the large contrast in

cyanide etching rate: no pits of significant depths are observed in areas not etched by the STM tip.

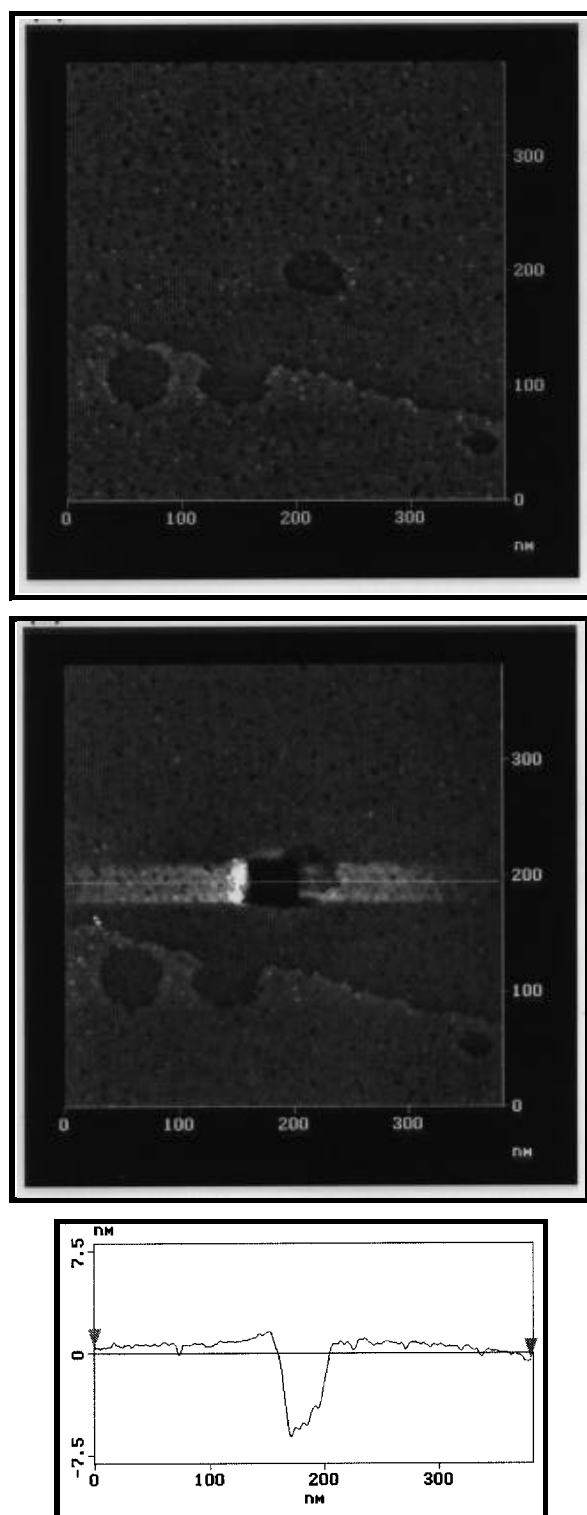


Figure 2: STM images of an Au(111) surface modified with a SAM of hexadecanethiol: (A) before and (B) after STM lithographic etch of a 50 nm \times 50 nm square window. (C) is a line profile indicated in (B). The z scale in both (A) and (B) is 5 nm, and darker shades stand for lower height.

The larger contrast for cyanide etching is not readily apparent since both Ag deposition and Au dissolution are electrochemical processes. The most reasonable explanation can be found in a study by Chailapakul *et al.* who showed that at the adventitious defect sites the rate of an electrochemical reaction is not only controlled by overpotential and intrinsic electron transfer rate, but also controlled by the size of a species involved in the electrochemical reaction.¹⁴ In our case, the size factor is important because cyanide ions have to completely penetrate an adventitious defect site in order to initiate the Au dissolution. In contrast, the conversion from Ag⁺ to Ag only requires electrons which can penetrate a defect site through quantum tunneling.

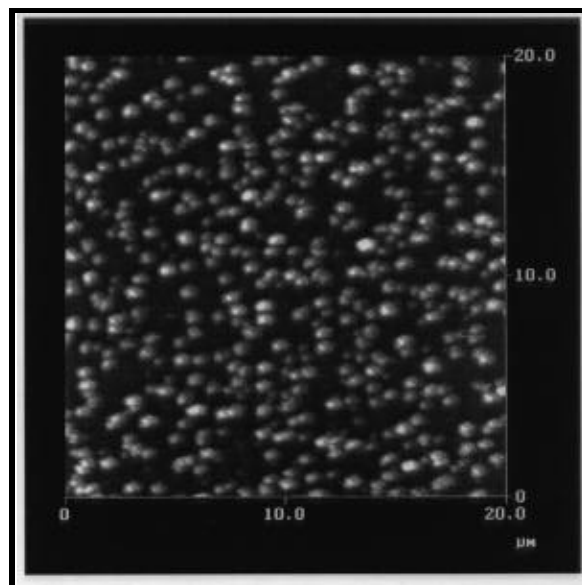


Figure 3: SFM image of Ag clusters deposited onto the adventitious defect sites at 200 mV deposition potential and with 10 s deposition time. The z scale is 0.5 μ m.

Figure 4A illustrates that a 500 nm tip-etched square has been enlarged by about 200 nm after cyanide etching. As expected, the amount of enlargement is reduced if shorter etching time is used. The triangular line cross section (Figure 4B) indicates an imaging artifact caused by the finite cone angle of the STM tip. Thus, the real depth of the etched pit may be deeper than the apparent depth. Figure 5 shows that the true depth can be measured if a larger square is created and that tip-etched patterns can be transferred to the underlying Au surface with high fidelity. This means that further improvement of the technique may allow us to fabricate more complex features. Kumar *et al.* have achieved similar feat using chemical cyanide etch and SAM-covered polycrystalline Au film patterned with an elastomeric stamp.¹⁵ Cyanide etching dramatically improves the contrast in the Ag deposition rate. There exists a window of threshold potential within which Ag deposition occurs only

at the tip-etched, cyanide-cleaned area but not at the adventitious defect sites (Figure 6).

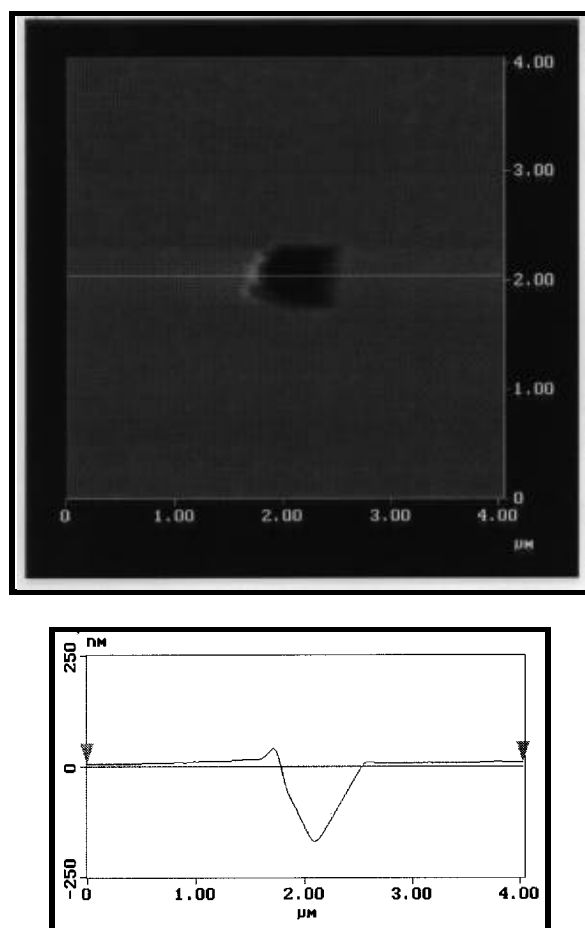


Figure 4: STM image and line profile of a tip-etched $500 \text{ nm} \times 500 \text{ nm}$ area after 3-min cyanide etching. The z scale is 200 nm .

The particle size in Figure 6 can be obtained by analyzing the line cross section of the corresponding SFM image. we have devised a simple method that takes into account the distortion due to the finite cone angle of a pyramidal SFM tip. A real particle is approximated as a hemispherical protrusion with its spherical center located a distance of q away from the Au surface (Figure 7). After a simple derivation based on geometric algebra, we obtain an equation which relates the radius of curvature r with three parameters that can be conveniently determined from an SFM image, namely, the half base-width d , the height h , and the cone angle α :

$$r = \frac{1}{1 - \sin \alpha} (d \cos \alpha - h \sin \alpha) - r_{\text{tip}} \quad (1)$$

where $\alpha = \arctan(d/h)$ and the tip radius of curvature r_{tip} can be ignored if it is much smaller than the particle's radius. The q value also gives us a rough estimate of particle shape. For example, $h = 2r$ and $q = r$ are expected for a sphere while $h = r$ and $q = 0$ for a hemisphere.

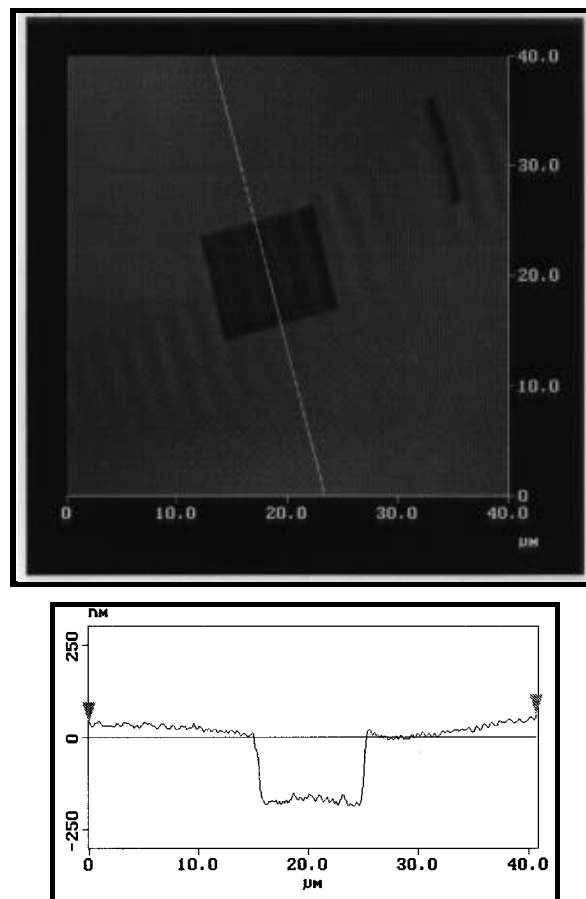


Figure 5: (A) SFM image of two features fabricated via STM lithography followed by 30 s cyanide etching: a $10 \mu\text{m} \times 10 \mu\text{m}$ square window and a $10 \mu\text{m}$ line. (B) line profile of the square window. The z scale is 500 nm .

Most Ag particles in Figure 6 are spherical, which suggests that Ag deposition may be a kinetically controlled process. This is within our expectation since the deposition potential for these particles are close to the thermodynamic threshold potential. One consequence of kinetically controlled growth, as seen in Figure 6, is that the particle size cannot be controlled easily because many factors can influence the growth rate. For example, growth rate would be sensitive to variations in the size or shape of a tip-etched area or the amount of trace organic adsorbates within the area. In comparison, Ag particles shown in Figure 3 are deposited at small defect sites under a large overpotential. These conditions favor a diffusion-controlled growth kinetics, which leads to a hemispherical particle shape. Hemispherical shape was also observed previously for copper particles deposited on a SAM-modified Au surface.¹⁷

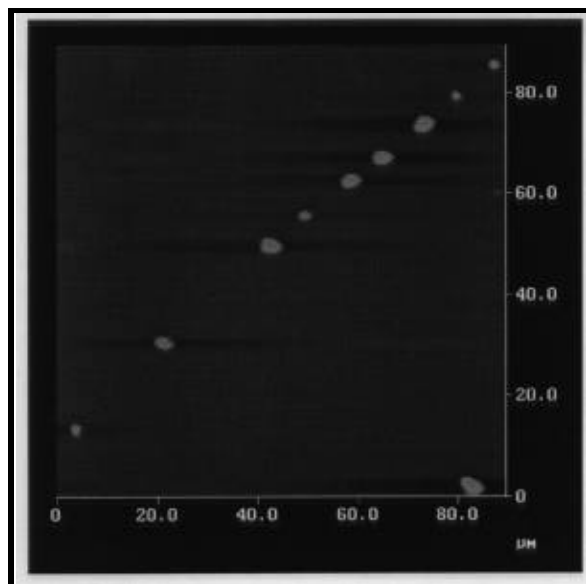


Figure 6: SFM image of a string of Ag particles deposited at tip-etched, cyanide-cleaned, and $100 \text{ nm} \times 100 \text{ nm}$ windows. The deposition was initiated at 470 mV for 3 min. The z scale is 500 nm. Particles appear bigger than their actual sizes because of tip shape and large image contrast.

The single particle fabrication technique outlined here has three distinct advantages for fabricating well-defined models. First, this technique allows unambiguous isolation of a single particle for optical measurements. The region surrounding each particle is atomically smooth Au(111) surface which is excellent for control studies. For example, smooth surface often does not support SERS, so we can be sure that a detected surface Raman signal is originated only from one desired Ag particle. Second, the size and the shape of the particle can be controlled by controlling the size and the shape of the lithographic area and by controlling the faradaic charge passed during the Ag deposition step. Due to the high spatial resolution of STM lithography, we expect that particles as small as 10 nm can be fabricated and characterized. Finally, the interparticle spacing can also be controlled by controlling the etched pit spacings during STM lithography. In the present study, we have demonstrated only the first advantage. It should be emphasized that our technique for fabricating single Ag particles can be applied also to other types of single particles such as semiconductor nano-particles if they can be deposited electrochemically.¹⁸ This would be a useful approach for correlating particle size, shape, and distribution with nanoparticle's optical properties such as bandgap and dynamic responses.^{1a}

SERS From Single Ag Particles

Quantitative analysis of SERS from *t*-4MMS adsorbed on single Ag particles, such as those shown in Figure 6, allows us to estimate the SERS enhancement factor.

According to EM enhancement theories, this factor is directly correlated with the enhancement of the near-field surrounding the Ag particles. The method for calculating enhancement factor has been outlined previously.³ The average result for single Ag particles is roughly 2×10^4 , which is much smaller than the expected enhancement factor of 10^6 measured with a large ensemble of particles, such as those shown in Figure 3.¹⁹ Thus, SERS signal due to a cluster of Ag particles is not simply the sum of signals from each individual particles. We propose that the extra enhancement is due to interactions between the EM field near closely-packed particles. Similar results have been observed previously in experiments that correlate SERS intensity and degree of colloid aggregation.²⁰ In addition, an EM model by Gersten and Nitzan also predicted that molecules located at the "gap sites" between two particles experience a stronger local EM field and resonance at a lower frequency than those for a single sphere.²¹

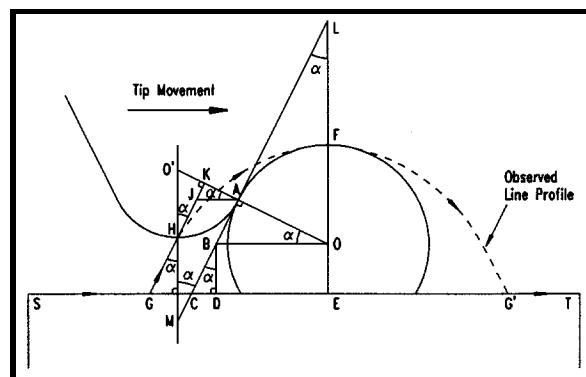


Figure 7: Determination of particle size from the mid-section line profile of an SFM image. The tip H moves from S-G-H-F-G'-T, producing the observed line profile. The contact point A shown here is an important location. Below A, the tip moves linearly along GH while the contact A slides along AL tangent to the surface of the spherical particle. Above A, the tip moves in a more complicated dashed trajectory. Equation (1) can be derived by noting some obvious identities: $r = OA$, $r_{tip} = O'A$, $q = OE = FE$, $FO = h$, r , and $d = GE$. Line GK is drawn through H and perpendicular to line O'O. All angles labeled as α are equal to the cone angle of the tip.

However, other possibilities are also likely to explain our quantitative results. First, a recent single particle SERS study revealed that ensemble-averaged enhancement factor is distributed inhomogeneously. Only a small percentage of the so-called "hot" particles contribute to the observed signal, and the exact cause for this is still unclear. Thus, our low single particle enhancement factors may be due to the low statistical probability for observing larger values. Second, particle size, shape, and surface chemistry are not controlled precisely in this study. SERS may be highly sensitive to these factors, which, in turn, will cause the inhomogeneity in SERS enhancement factor.

In conclusion, we have demonstrated here a new technique for fabricating single Ag nanoparticles, which pro-

mises precise control over particle size, shape, and spatial configuration. We have detected for the first time surface-enhanced Raman scattering due to single isolated Ag particle with essentially no background interference from the surface surrounding the particle. Finally, we have observed extra enhancement due to particle clustering and have attributed it to the enhancement of the EM field at the "gap sites" between closely-packed particles.

Acknowledgments

L. S. gratefully acknowledges financial support from National Science Foundation (CHE-9531243). This work was initially supported by the University of Minnesota start-up funds.

Notes and References

1. See, for example, Alivisatos, A. P. *J. Phys. Chem.* 1996, **100**, 13226-13239. Brus, L. E. *Appl. Phys.* 1991, **53**, 465-474. Brinker, C. J.; Scherer, G. W. *Sol-Gel Science*; Academic Press: San Diego, CA, 1990. Gao, W.; Reven, L. *Langmuir* 1995, **11**, 1860. *Better Ceramics Through Chemistry, III*; Brinker, C. J., Clark, D. E., Ulrich, D. R., Eds.; *Mat. Res. Soc.*: Pittsburgh, PA, 1988.
2. (a) Birke, R. L.; Lu, T.; Lombardi, J. R. in *Techniques for Characterization of Electrodes and Electrochemical Processes*; Varma, R., Shelman, J. R., Eds.; Wiley: New York, 1991. (b) Moskovits, M. *Reviews of Modern Physics* 1985, **57**, 783. (c) Schatz, G. C. *Acc. Chem. Res.* 1984, **17**, 370-376. (d) Campion, A.; Ivanecy III, J. E.; Child, C. M.; Foster, M. *J. Am. Chem. Soc.* 1995, **117**, 11807-11808.
3. Xiao, T.; Ye, Q.; Sun, L. *J. Phys. Chem. B* 1997, **101**, 632-638.
4. Nie, S.; Emory, S. R. *Science* 1997, **275**, 1102-1106.
5. Sonnenfeld, R.; Schneir, J.; Hansma, P. K. in *Modern Aspects of Electrochemistry*; White, R. E., Bockris, J. O'M., Conway, B. E., Eds.; Plenum: New York, 1990.
6. (a) Hsu, T. *Ultramicroscopy* 1983, **11**, 167. (b) Schott, J. H.; White, H. S. *Langmuir* 1992, **8**, 1955-1960.
7. Ross, C. B.; Sun, L.; Crooks, R. M. *Langmuir* 1993, **9**, 632-636.
8. Sun, L.; Crooks, R. M. *Langmuir* 1993, **9**, 1951-1954.
9. (a) Schönenberger, C.; Sondag-Huethorst, J. A. M.; Jorritsma, J.; Fokkink, G. J. *Langmuir* 1994, **10**, 611-614. (b) Edinger, K.; Gölzhäuser, Demota, K.; Wöll, Ch.; Grunze, M. *Langmuir* 1993, **9**, 4-8. (c) Chailapakul, O.; Sun, L.; Xu, C.; Crooks, R. M. *J. Am. Chem. Soc.* 1993, **115**, 12459-12467.
10. Poirier, G. E.; Pylant, E. D. *Science* 1996, **272**, 1145-1148.
11. Schoer, J. K.; Zamborini, F. P.; Crooks, R. M. *J. Phys. Chem.* 1996, **100**, 11086-11091.
12. Pioneer Press, St. Paul, MN, 1995.
13. Johnson, D. C.; LaCourse, W. R. *Anal. Chem.* 1990, **62**, 589A-596A.
14. Chailapakul, O.; Crooks, R. M. *Langmuir* 1993, **9**, 884-888.
15. Kumar, A.; Biebuyck, H. A.; Whitesides, G. M. *Langmuir* 1994, **10**, 1498-1511.
16. The deposition potential appears to be higher than the thermodynamic threshold of 425 mV by an amount that seems too large to attribute to measurement uncertainties. This may be caused by liquid junction potential and other factors associated with a non-ideal reference electrode.
17. Sondag-Huethorst, J. A. M.; Fokkink, L. G. J. *Langmuir* 1995, **11**, 4823-4831.
18. Golan, Y.; Margulis, L.; Rubinstein, I.; Hodes, G. *Langmuir* 1992, **8**, 749-752.
19. To quantify SERS intensity, we used the integrated peak area of two vibrational modes from *t*-4MMS. These modes are located at 1587 cm⁻¹ and 1626 cm⁻¹, corresponding to the phenyl ring C=C stretching vibration and the ethylene C=C stretching vibration, respectively. The assignment was found in Baranovic, G.; Meic, Z.; Gusten, H.; Mink, J.; Keresztury, G. *J. Phys. Chem.* 1990, **94**, 2833-2843.
20. Blatchford, C. G.; Campbell, J. R.; Creighton, J. A. *Surf. Sci.* 1982, **120**, 435-455. Sun, L., Ph.D. Thesis, Northwestern University, Evanston, IL, 1990.
21. Gersten, J. I.; Nitzan, A. *Surf. Sci.* 1985, **158**, 165-189.